The Boreal Summer Zonal Wavenumber-3 Trend Pattern and Its Connection with Surface Enhanced Warming

YUSEN LIU,[a] CHENG SUN,[a] AND JIANPING LI[b,c]

[a] College of Global Change and Earth System Science (GCESS), Beijing Normal University, Beijing, China
[b] Frontiers Science Center for Deep Ocean Multispheres and Earth System (FDOMES), Key Laboratory of Physical Oceanography, Institute for Advanced Ocean Studies, Ocean University of China, Qingdao, China
[c] Laboratory for Ocean Dynamics and Climate, Pilot Qingdao National Laboratory for Marine Science and Technology, Qingdao, China

(Manuscript received 17 June 2021, in final form 21 September 2021)

ABSTRACT: The Northern Hemisphere warms faster under global warming and suffers from more frequent heatwaves, causing considerable social and economic damage. The Northern Hemisphere surface warming exhibits strong regionality, with multiple "hotspots" (areas of enhanced warming), but the relations among them remain unclear. This study finds a dominating zonal wavenumber-3 (ZW3) trend pattern in the upper-level geopotential heights during the boreal summer. The summer geopotential heights show significant increasing trends along the latitudinal circle around 60°N, with three centers located over northeastern America, western Eurasia, and eastern Siberia. The regionally enhanced surface warming trends are closely linked to the increased geopotential through the reduced cloud cover, exhibiting a consistent ZW3 pattern. The model simulations forced by sea surface temperature (SST) and Arctic sea ice cover (SIC) indicate that the SST forcing plays an important role in generating the ZW3 pattern, while the contribution of the SIC is minimal. A theoretical barotropic model can fairly well reproduce the observed ZW3 structure forced by a heating source located over the subtropical North Atlantic, where the SSTs show prominent warming trends and a close relationship with the ZW3 pattern. Our results indicate that the hotspots may be interconnected and are related to a Rossby wave train with a ZW3 structure. It highlights a vital role of tropical/subtropical SSTs on the atmospheric circulation and the associated surface enhanced warming over the mid- to high latitudes, which may have great implications for the coordinated heatwave events and tropical–extratropical teleconnections.

KEYWORDS: Atmosphere-ocean interaction; Atmospheric circulation; Planetary waves; Teleconnections; Extreme events; Sea ice

1. Introduction

The global mean surface temperature has increased substantially by about 1°C since 1900, with a more rapid warming rate of +0.18°C decade^{-1} since 1981 (Hartmann et al. 2013). In addition to the mean global warming, it also exhibits strong regionalities. A faster warming rate is shown in the Northern Hemisphere than over the Southern Hemisphere, and land is usually heated more intensely than the ocean (Sutton et al. 2007). A minor change that took place in the mean state is deemed to cause a significant shift in extremes (Field et al. 2012; Perkins 2015). Over the past decades, record-breaking warming events have been witnessed around the globe. Observational evidence also indicates that the summer climate in Europe has been warming at a very high rate in recent decades, associated with pronounced trends in temperature extremes (Boé et al. 2020; Klein Tank and Können 2003). East Asia and North America are also exposed to the threat of extremely high temperatures over the years (Qian et al. 2020; Wu et al. 2012b). Those regions are highly populated and active in economic activities and thus are more vulnerable to such temperature extremes. Moreover, in the context of future global warming, such events will be more frequent and more intense (Hartmann et al. 2013; Meehl and Tebaldi 2004), causing considerable damage to human society and natural environment. Therefore, it is of importance to evaluate both global and regional enhanced warming trends and investigate their causes and potential linkages under the circumstances of mean temperature rise.

Rising atmospheric greenhouse gas concentrations are the main reason for the recently enhanced heat extremes (Christidis et al. 2005; Stott et al. 2000; Tett et al. 2002). For example, the increase in greenhouse gas concentrations could exacerbate the variability of summer temperatures in Europe (Stott et al. 2004), leading to higher frequency, longer duration, and more intense warming events (Fischer and Schar 2009, 2010). Several studies have also analyzed the characteristics of extreme events in the context of future global warming of 1.5° and 2°C using climate model simulations (Dosio et al. 2018). The 2°C level of global warming would significantly increase global extreme heatwave events compared to 1.5°C.

In addition to the greenhouse effect, atmospheric circulation and land–atmosphere interactions are fundamental factors causing above-average surface warming trends in the

Denotes content that is immediately available upon publication as open access.

Supplemental information related to this paper is available at the Journals Online website: https://doi.org/10.1175/JCLI-D-21-0460.s1.

Corresponding author: Cheng Sun, scheng@bnu.edu.cn

DOI: 10.1175/JCLI-D-21-0460.1

Northern Hemisphere (Kysely 2007; Kysely and Domonkos 2006). A persistent high pressure system favors the development and maintenance of high temperature via prevalent descending motions, and the heat released during the sinking motion is conducive to surface heating. Meanwhile, divergent flow associated with high pressure reduces cloud and increases the downward shortwave radiation on the ground, heating the surface directly, which is also conducive to extreme high-temperature events. For instance, it is suggested that the high pressure system contributed to the 2003 European heatwave (Tomczyk et al. 2017). In addition to large-scale circulation systems, anomalies in land surface conditions also have an important influence on the recent enhanced warming trend (Fischer et al. 2007a). Abnormal reduction of soil moisture can weaken the cooling effect caused by latent heat release, which in turn leads to surface warming (Fischer et al. 2007b). Also, snow cover is suggested to enhance heatwave activity via inducing changes in atmospheric circulation and reduced albedo (Wu et al. 2012a).

Another important factor in Northern Hemisphere high temperature extremes is sea surface temperature (SST) associated with internal atmospheric variability (Perkins-Kirkpatrick et al. 2017). Previous studies have demonstrated that global land warming is partly caused by ocean heating through moisture–radiation feedbacks rather than a direct response to increasing greenhouse gases alone (e.g., Compo and Sardeshmukh 2009). Pan-tropical SST variability strongly modulates the heatwave activity across the Northern Hemisphere through anomalous atmospheric circulation. The occurrence of heatwave events in the European region is closely linked to the anomalous warming of the equatorial Atlantic Ocean (Cassou et al. 2005; Della-Marta et al. 2007; Sutton and Hodson 2005). For the East Asian region, a previous study has shown that summer temperature in China is connected with SST anomalies over the Indian Ocean by the anomalous large-scale atmospheric circulation (Hu et al. 2011). Meanwhile, the surface air temperature and related extremes are also influenced by some predominant climate modes (e.g., MJO, mega-ENSO, and AMO) (Hsu et al. 2020; Zhou and Wu 2016). In addition, a strong correlation is observed between the interdecadal pattern of North American heatwave frequency and the spring SST anomaly in the tropical Atlantic and western Pacific (Wu et al. 2012b). Above all, other studies also demonstrate the importance of Arctic sea ice cover (SIC) on the Northern Hemisphere temperature as the combined effects of SST/SIC could explain about 62.2% of the Eurasian air temperature warming trend (Dong et al. 2017). The summer Arctic sea ice has been witnessing a rapid shrinking trend during the recent decades (Cai et al. 2021). A good relationship has been found between the Arctic sea ice loss and summer north-central United States air temperature (Budikova et al. 2017). The Arctic sea ice loss changes surface albedo and allows more absorption of shortwave radiation, causing faster heating than other latitudes, which is called Arctic amplification (Serreze et al. 2009; Stroeve et al. 2012). The Arctic amplification is linked to the midlatitude extreme weather events, as revealed by previous studies (Cohen et al. 2014; Coumou et al. 2018). Due to the reduction in SIC, the temperature gradient between the Arctic and lower latitudes declines, which amplifies the midlatitude wave activity and associated circulation anomalies (Overland and Wang 2010), resulting in an increase in surface air temperature and heat extremes. On the other hand, there are some disagreements regarding whether the Arctic sea ice loss suppresses midlatitude warming (Wu et al. 2016), and the relative role of SIC in comparison with SST in the recent enhanced warming trend remains elusive.

A previous study indicated that the Northern Hemisphere "hotspots" located in western Europe, northern East Asia, and North America exhibit coherent patterns, which may be further regulated by the Atlantic multidecadal oscillation (AMO) (Gao et al. 2019). It raises the question of whether these enhanced warming events are independent. If not, how are they connected? Previous studies have found a potential linkage between the mid- to high-latitude Rossby wave and Northern Hemisphere heatwave activity. It is suggested that an anomalous Rossby wave with wavenumber 5 is responsible for U.S. heatwaves (Teng et al. 2013), which implies an important role of internal atmospheric dynamics on heatwave events rather than thermal processes alone. Indeed, a circumglobal teleconnection (CGT), with a wavenumber-5 structure, is thought to influence the Northern Hemisphere summertime surface air temperature (Ding and Wang 2005). The CGT exhibits a phase-locked pattern, and the geographic centers generally correspond with the aforementioned hotspots, indicating that the recent enhanced warming trends are likely interconnected via atmospheric planetary waves. In the light of CGT, previous studies have investigated the relationship between the amplified Rossby waves and regional temperature extremes (Screen and Simmonds 2014). The zonal wavenumber-5–8 patterns generated through the quasi-resonant amplification (QRA) mechanism (Kornhuber et al. 2017a; Kornhuber et al. 2017b) have been investigated and proved to influence extreme high temperature events (Coumou et al. 2014; Kornhuber et al. 2019) on the synoptic time scale. However, it is still not fully understood how the planetary wave interacts with surface warming on the interannual and interdecadal time scale. A previous study has illustrated the zonal wavenumber-3 pattern in the Northern Hemisphere winter (Teng and Branstator 2012). Does wavenumber-3 pattern also exist during boreal summer? If so, how are hotspots interconnected via the planetary wave mechanism on interannual and longer time scales?

This study investigates the zonal wavenumber-3 trend pattern in the Northern Hemisphere summer and links it with the recent warming trends over the aforementioned hotspots. Considering that the mid- to high-latitude SAT may be modulated by SST and SIC, we further evaluate the relative role of SST and SIC in causing the zonal wavenumber-3 trend pattern during boreal summer.

2. Data and methods

This study uses the Modern-Era Retrospective Analysis for Research and Applications (MERRA) from NASA's Global

Modeling and Assimilation Office (Rienecker et al. 2011) and the Japanese 55-year Reanalysis (JRA-55) from the Japan Meteorological Agency (Kobayashi et al. 2015). The ERA5 data (Hersbach et al. 2020) are also employed for comparison. The land surface temperature data are from HadCRUT4 (Morice et al. 2012), derived from the Met Office Hadley Centre. The heatwave quantities are calculated based on the HadGHCND maximum daily temperature data extending from 1950 to 2014. The methods for defining a heatwave and the metrics are consistent with the previous studies (Perkins-Kirkpatrick and Lewis 2020; Perkins and Alexander 2013). We define a heatwave when at least three consecutive days are above the 90th percentile of maximum temperature for each calendar day. The percentile is calculated on a 15-day running window of daily maximum temperatures over 1961–90. Heatwave frequency is defined as the sum of all heatwave days and heatwave amplitude (the peak daily maximum temperature in the hottest heatwave). In addition, the SST data from the ERSST version 5 dataset are also used (Huang et al. 2017). All data are employed for the period 1982–2013 for comparing the multidecadal trends among different datasets, and the assessment of the model simulations ends in 2013. The results are largely similar if we extend the trend analysis over a longer time period (1960–2018; see Fig. 1 in the online supplemental material). The trend analysis is calculated over the JJA (June–August) mean to isolate the features of trends during the boreal summer.

We conducted two experiments to distinguish the relative influences of SST and SIC on atmospheric zonal wave patterns, referred to as SST-SIC-EXP and SIC-EXP. In the SST-SIC-EXP simulation, the model is prescribed with the observed daily-varying Arctic sea ice and global SSTs derived from the National Oceanic and Atmospheric Administration (NOAA) high-resolution blended analysis of daily SST and ice (OISST version 2) (Reynolds et al. 2007). In the SIC-EXP, the model is forced by the observed daily-varying Arctic sea ice and climatological SST. The sea ice data obtained from Cavalieri et al. (1996) and Grumbine (1996) are used for the period before and after 2005, respectively. The configuration of Arctic sea ice and SST in the SIC-EXP simulation is consistent with the previous studies (Sun et al. 2020). This experiment aims to inspect the direct influence of the Arctic sea ice on the atmospheric circulation and associated zonal wave patterns, while the changes in SST indirectly related to the Arctic sea ice are not taken into account.

The two experiments are performed under the NordForsk funded GREENICE project (https://greenice.w.uib.no/about/) (Ogawa et al. 2018), using the Community Atmosphere Model (CAM4) (Neale et al. 2013), which contains 26 vertical levels (up to 3 hPa), with a horizontal resolution of $0.9° \times 1.25°$. The model is prescribed with the transient external forcing, consistent with the historical radiative forcing following the Atmospheric Model Intercomparison Project (AMIP) protocol. We employ an ensemble of 20 members to better highlight the forced component of the atmospheric circulation (in response to the SST or SIC) in the simulations, and the ensemble mean is derived for analysis. The simulation data (SST-SIC-EXP and SIC-EXP) are publicly available and derived from https://wiki.uib.no/greenice/index.php/Main_Page for the period 1982–2013.

We also construct a barotropic model to investigate the responses of the mid- to high-latitude atmosphere to subtropical perturbations (Ting 1996). The model is based on the vorticity equation and can be linearized about the basic mean state when the model is applied at a single level with a horizontal resolution of T42:

$$J(\bar{\psi}, \nabla^2\psi') + J\left(\psi', \nabla^2\bar{\psi} + f\right) + \nu\nabla^6\psi' + \alpha\nabla^2\psi' = S',$$

where J represents a Jacobian operator, $\bar{\psi}$ and ψ' are basic state and perturbation streamfunctions, respectively, f is the Coriolis parameter, and S' is the anomalous vorticity source induced by the divergence associated with the direct diabetic heating and the ascending motion (Ting 1996); also, υ is the biharmonic diffusion coefficient (set to 2×10^{16} m^4 s^{-1}) in order to dampen small-scale eddies and α is Rayleigh friction (set to 10^{-1} days). According to the previous study, the barotropic model is linearized about the basic mean flow at 500 hPa, which is the equivalent barotropic level for the summer season as suggested in (Ting 1996).

In this study, the linear trends are calculated using the robust Theil–Sen trend estimation method (Sen 1968), which is more accurate than simple linear regression and insensitive to outliers compared with the least squares method. The trends are tested by applying the nonparametric Mann–Kendall method. This method has been widely used in previous studies and proved to be effective and accurate (Sun et al. 2019). In addition, we apply the Fourier decomposition method on the trend fields to inspect the zonal harmonic patterns over the mid- to high latitudes. The predominant zonal wavenumber is determined by the amplitude squared of zonal harmonics from 1–5 during the boreal summer (JJA).

3. Results

a. *Patterns of trend in summer zonal waves and the associated warming*

We calculate the trends in 500- and 200-hPa geopotential heights (shading in Fig. 1) based on the MERRA dataset. The 500-hPa trend field displays multiple increase centers with slight decline trends located in between (Fig. 1a). The most prominent uplifts in geopotential height are found over the northeastern North America and Greenland region, Europe, the Mongolian Plateau, and the eastern Siberia and North Pacific region. Along the 60°N latitude circle, these active centers tend to modify the climatological troughs and ridges. For instance, the troughs over the east coast of North America and northern East Asia are weakened by the long-term increasing trend, while the trough over western Siberia tends to intensify due to the decline in geopotential heights. The trend in 200-hPa geopotential height exhibits a similar pattern (Fig. 1b), as the four increase centers correspond well, indicating a barotropic structure of the long-term trend. The geopotential height at the 200-hPa level shows a more intense increasing trend, and the active centers are stronger than at

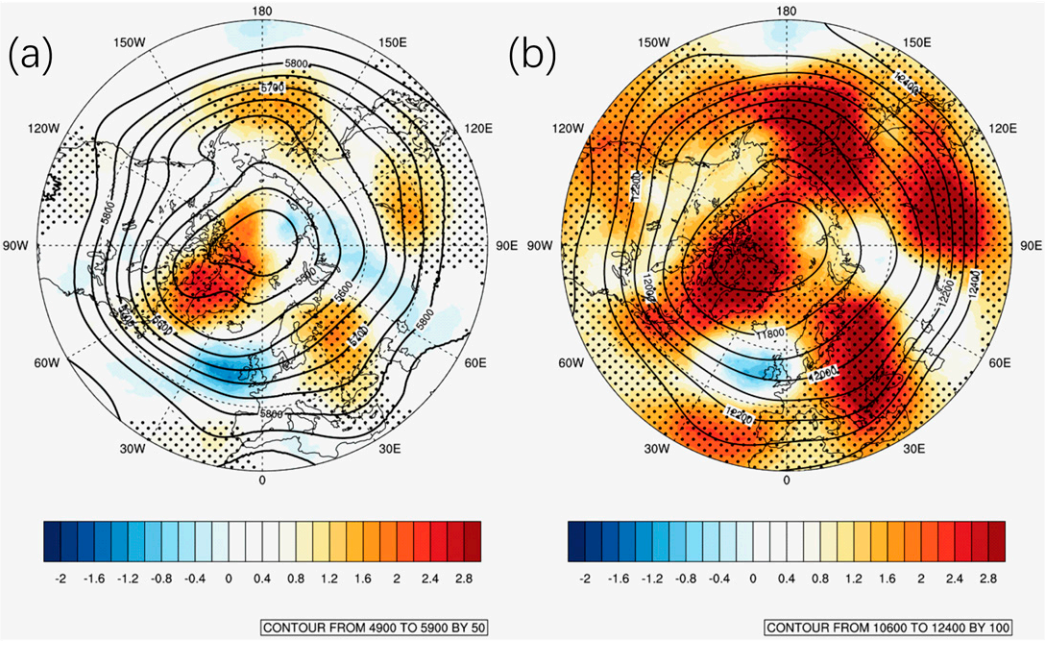

FIG. 1. The climatology (contours; unit: m) and long-term trend (shading; unit: m yr^{-1}) of geopotential heights at the (a) 500- and (b) 200-hPa levels during the boreal summer, using the MERRA data. The long-term trend is calculated for the period 1982–2013. The stippling indicates the trends that are significant at the 95% confidence level.

the lower level, together with extended spatial coverage. We also inspect the trend in 500- and 200-hPa geopotential heights using JRA-55 (see supplemental Fig. 2) and the spatial patterns are consistent. Moreover, the trend patterns also agree with previous study (Horton et al. 2015). The above results indicate that the trend of geopotential height over the mid- to high-latitude atmosphere exhibits significant zonal fluctuations, which are independent of data selection.

To investigate the characteristic of the fluctuations in upper-level geopotential height, we then apply the Fourier decomposition method on the trend and climatology fields of the 200- and 500-hPa geopotential heights. The amplitudes of each zonal harmonic over latitudes are displayed in Fig. 2. The climatological geopotential height (Fig. 2a) mainly exhibits zonal wavenumber-1 patterns at both the 200-hPa (shading) and 500-hPa (contours) levels. The zonal wavenumber-1 pattern is most significant at the higher latitudes (north of 60°N) as well as the subtropical region due to the land–sea distribution and complex terrain. A zonal wavenumber 3 can be found near 60°N, but it is rather weak at the upper troposphere. This suggests that the climatology of the Northern Hemisphere geopotential height is likely dominated by the zonal wavenumber-1 pattern, which is consistent with that in the JRA-55 data (supplemental Fig. 3a). By decomposing the trend pattern, we may find that the upper-level troposphere, especially for the level of 200 hPa (shading), is dominated by a zonal wavenumber-3 (ZW3) pattern (Fig. 2b). It is basically confined to the latitudes of 60°N ± 8°. The ZW3 pattern corresponds with the increasing trends of geopotential heights over northeastern North America, Europe, and eastern Siberia, which are statistically significant at the 95% confidence level. It suggests that strong fluctuations indeed exist in the geopotential height trends and exhibit a prominent ZW3 characteristic. Similar results can be found using the JRA-55 data (see supplemental Fig. 3b). Corresponding to the geopotential height, we also examine wavenumber 3 in 200-hPa meridional winds. The spatial trend pattern (not shown here) is consistent with that shown in Fig. 1, and the amplitude of the decomposed harmonic 3 prevails (supplemental Fig. 4). It suggests that the ZW3 pattern can be identified in both geopotential and meridional winds. The above results are consistently found in the ERA5 (supplemental Fig. 5).

We also find that the ZW3 pattern not only exists in the long-term trend but also is a prominent pattern of interannual variability. The leading empirical orthogonal function (EOF1) pattern of the 200-hPa geopotential height (supplemental Fig. 6a) exhibits a significant wave train pattern across the mid- to high-latitude Northern Hemisphere, consistent with the observed trend patterns in Fig. 1. Using the Fourier decomposition method, the amplitude of the harmonic 3 is most prominent in the EOF1 pattern (supplemental Fig. 6d), indicating that the ZW3 pattern is still robust over variability. The correlation map between the 200-geopotential height and the time series corresponding with EOF1 is further examined (supplemental Fig. 6c). There are three significant centers of action located over northeastern North America, Europe, and eastern Siberia, indicating that the ZW3 is a phase-locked pattern and its active centers are prominent over interannual variability. It must be noted that the correlation is insignificant over Mongolia, indicating that the coherence of the increased geopotential height in Mongolia with the ZW3 pattern is rather weak at interannual variability. For the EOF1 of detrended data (supplemental Figs. 6b and 6e), the spatial

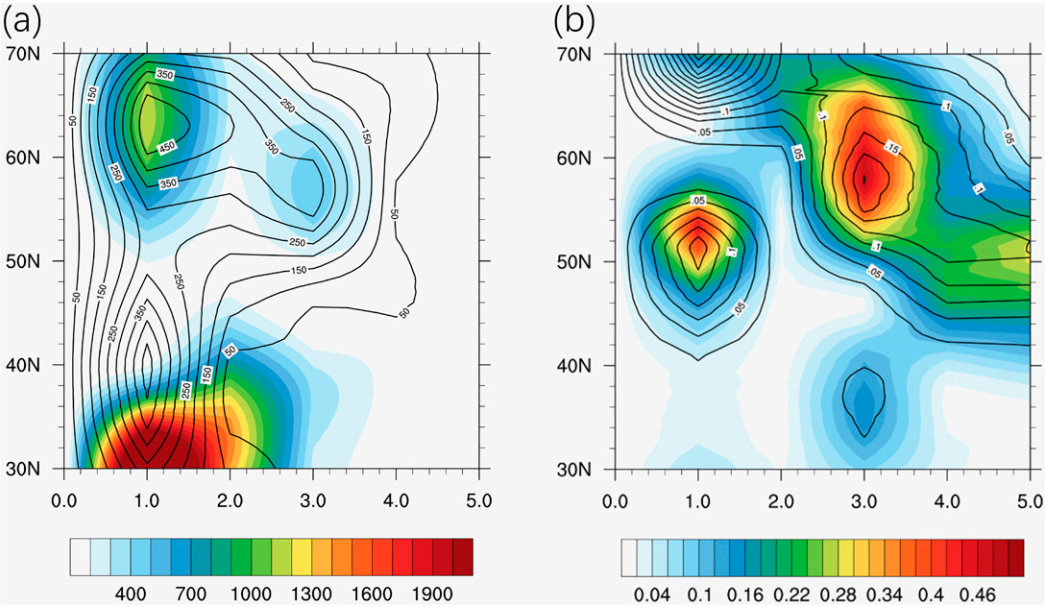

FIG. 2. The amplitude squared of zonal harmonics 1–5 of the boreal summer geopotential heights (a) climatology (unit: m^2) and (b) long-term trend at the 500-hPa level (contours) and 200-hPa level (shading) (unit: $m^2\ yr^{-2}$) using the MERRA data.

pattern is somewhat similar to that observed, and the decomposed wavenumber 3 still prevails over other harmonics. The above analysis provides statistical evidence that the ZW3 is a prominent pattern of both trend and interannual variability in atmospheric circulation during the boreal summer.

In addition, wave flux analysis (see appendix A) based on JRA-55 data is carried out to examine the underlying physics of Rossby wave energy propagation associated with the ZW3. As shown in supplemental Fig. 7a, a significant zonal wave train at 200 hPa is found over the mid- to high latitudes, preferentially at a wavenumber of 3, propagating eastward. The wave train consists of three active centers (the North America and Greenland region, Europe, and eastern Siberia) connected by strong wave fluxes. The wave flux pathway is confined near 60°N, and the branches toward lower latitudes are rather weak and insignificant compared to the zonal propagation. The wave train is also significant at 500 hPa, exhibiting a ZW3 pattern (supplemental Fig. 7b). The wave flux indicates strong connectivity among these centers, further verifying an eastward dispersion of Rossby wave energy. The above results conclude that the existence of zonally propagating ZW3 is supported by basic Rossby wave propagation theories. It is statistically significant and physically robust.

The increased geopotential height corresponds with more descending motions, inducing air temperature warming due to adiabatic heating and increases in the cloud-related downward shortwave radiation. Thus, we inspect the trend in 850-hPa air temperature and its zonal fluctuations. The air temperature using the MERRA dataset (Fig. 3a) exhibits strong and significant warming over the northeastern North America and Greenland region, Europe, and eastern Siberia, corresponding well with the increasing trend in geopotential heights. Similarly, the air temperature also has zonal fluctuations over the mid- to high latitudes. More importantly, the zonally decomposed air temperature shows a prominent wavenumber-3 pattern near 60°N latitude (Fig. 3b), consistent with that in geopotential heights. We may notice that the warming trends are not limited to the high-latitude regions but also extend south to the areas like western North America, the Black Sea, and the Mongolian Plateau. Thus, the zonal harmonics with a wavenumber larger than 3 may relate to the lower-latitude fluctuations. In the JRA-55 dataset, the trend pattern is overall consistent, exhibiting an even more prominent ZW3 pattern (supplemental Fig. 8). Based on the above analysis, we may infer that the significant warming centers over the mid- to high latitudes (approximately confined to the range of 60°N ± 8°) are likely interconnected via the zonal wave activity (supplemental Fig. 7), forming a ZW3 pattern in both geopotential height and air temperature.

To further confirm the existence of the ZW3 pattern, we calculate the long-term trend in surface air temperature (SAT) using the HadCRUT data (Fig. 4a). There are three warming centers, located in the northeastern North America and Greenland region, Europe, and Mongolia, that resemble the air temperature pattern at 850 hPa. In addition, the warming trend over eastern Siberia is relatively weak but still statistically significant. At higher latitudes (north of 50°N), the zonal fluctuation in SAT is prominent, which can be well interpreted by the trends in geopotential height. As shown in Fig. 1, the geopotential heights increase significantly over northeastern North America and Greenland. For the northern Eurasian continent (along 60°N latitude), the geopotential heights also exhibit increasing trends over Europe and eastern Siberia, with a decreasing trend in between. Thus, the SAT

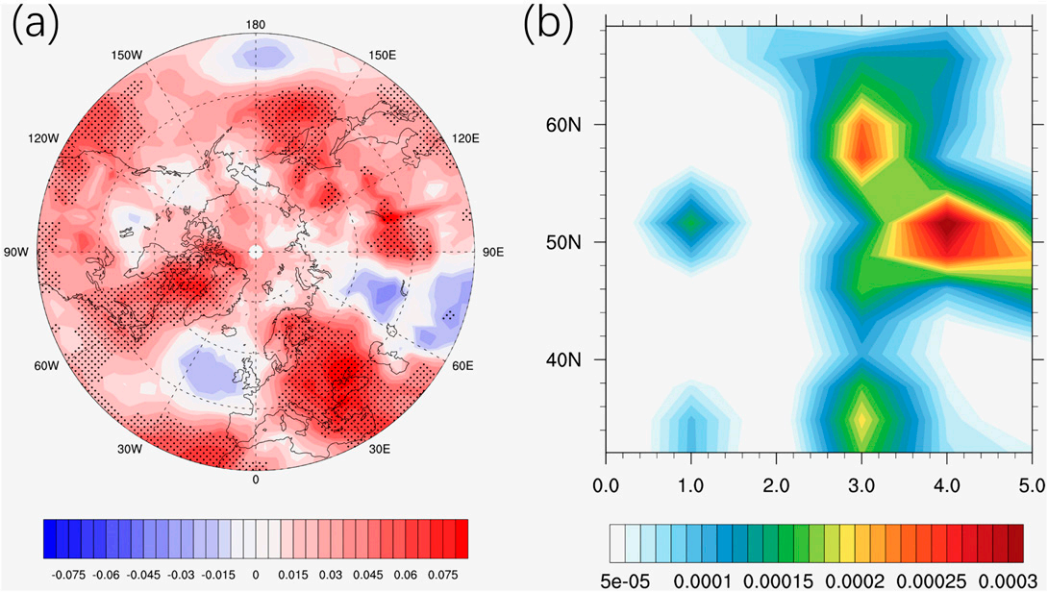

FIG. 3. (a) The trends in summer 850-hPa air temperature (unit: K yr^{-1}) and (b) the corresponding amplitude squared of zonal harmonics 1–5 (unit: K^2 yr^{-2}), using the MERRA data. The long-term trend is calculated for the period 1982–2013. The stippling indicates trends that are significant at the 95% confidence level.

warming trend centers well correspond with the trends in atmospheric circulation, which exhibits a significant ZW3 pattern. We also examine the trend in cloud cover (Fig. 4b). It is likely that the intensified descending motions associated with geopotential heights lead to anomalously low cloudiness, which tends to amplify the net downward shortwave radiation, resulting in long-term warming trends over the high-latitude regions. Moreover, the SAT trend would also exhibit zonal fluctuations to some extent, corresponding to the ZW3 pattern in the atmospheric circulation. Note that the reduction in cloudiness over eastern Siberia is not as significant as in Europe and Mongolia. This is due primarily to the relatively weak increase in geopotential height over the inland regions. Accordingly, the warming over northeastern Siberia

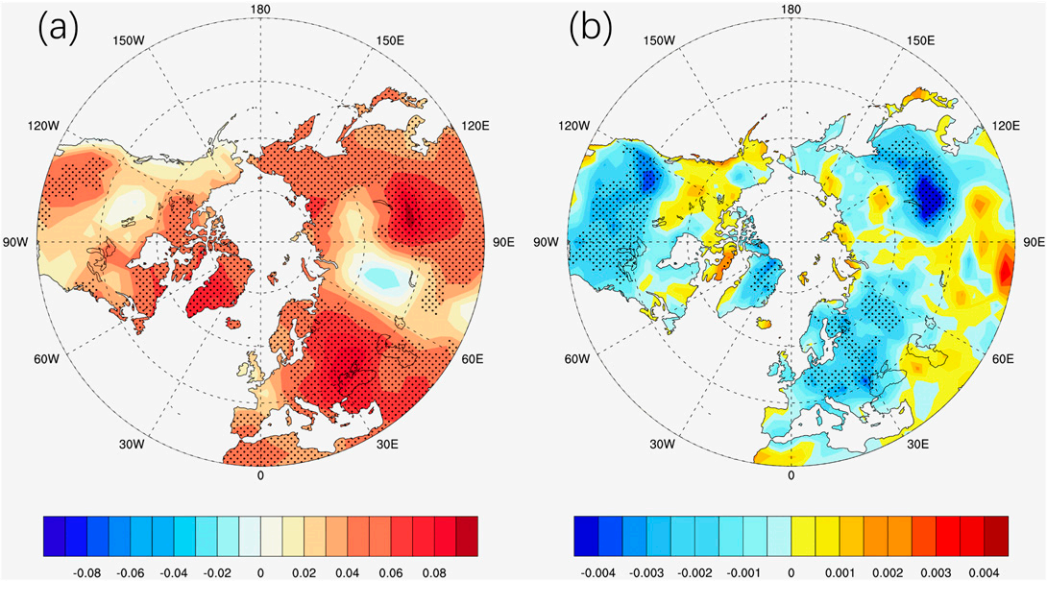

FIG. 4. (a) The trend of summer surface air temperature (unit: K yr^{-1}) derived from the HadCRUT data for the period 1982–2013. (b) The trend of cloudiness (unit: yr^{-1}) in the MERRA data. The stippling indicates trends that are significant at the 95% confidence level.

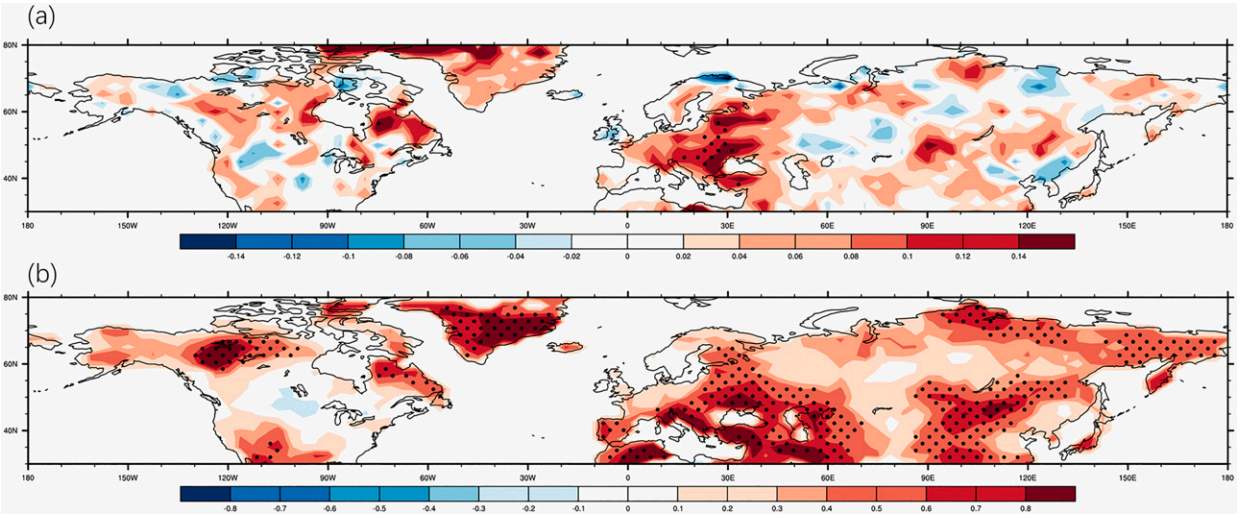

FIG. 5. The long-term trends in (a) heatwave amplitude (K yr^{-1}) and (b) heatwave frequency (days yr^{-1}) during the boreal summer. The long-term trend is calculated for the period 1982–2013. The stippling indicates trends that are significant at the 95% confidence level.

is also not that intense. Nevertheless, it is noticeable that the zonal fluctuation in SAT is still prominent, and the eastern Siberia warming trend is an essential part, exhibiting a consistent ZW3 pattern near 60°N latitude. We may conclude that the zonal wave activity found in geopotential height (supplemental Fig. 7) is able to explain the recent surface warming trends via cloud-radiation feedback. It is likely a different approach for understanding the interconnectivity of the surface warming trends and the associated temperature extremes.

As suggested in previous studies, the shifts in mean surface temperature would inevitably induce changes in extremes, such as heatwave activity (Field et al. 2012; Perkins 2015). In recent years, the Northern Hemisphere has been repeatedly subject to severe heatwaves. Here, the relationship between the ZW3 and heatwave activity is inspected. As shown in Fig. 5, the heatwave amplitude and frequency exhibit overall increasing trends, together with a few enhanced centers. Interestingly, the heatwave amplitude (Fig. 5a) centers in the northeastern North America and Greenland region and in Europe, corresponding to the enhanced warming in SAT and the increased geopotential heights. For the heatwave frequency (Fig. 5b), the increasing trends over Greenland, Europe, and eastern Siberia are prominent and statistically significant. These two heatwave quantities both indicate a close connection with the SAT, which exhibits a wavenumber-3 pattern. The spatial patterns of heatwave quantities are in good agreement with the upper-level tropospheric zonal fluctuations, given implications of the interconnections among these heatwave active centers located over the Northern Hemisphere mid- to high latitudes. The ZW3 pattern found in the upper-level geopotential height has profound influences on the surface enhanced warming trends as well as the temperature extremes. Although the heatwave activity and the increased geopotential height correspond well, the causes of enhanced heatwave intensity and frequency are not conclusive. It must be noted that the feedback of local land–atmosphere interaction may also play a role in land surface warming and the associated heatwave activity (Chen et al. 2020; Hong et al. 2017; Zhou et al. 2015, 2016). In addition, the ZW3-related descending motions could initiate a series of reactions of the land ecosystem that further intensify surface warming.

b. *Role of SST/SIC in causing the zonal wavenumber-3 trend pattern*

The long-term trends in geopotential heights exhibit significant zonal fluctuations. The zonal wave activity is dominated by a wavenumber-3 pattern along 60°N latitude, linking the SAT warming trends and heatwave activities through the alternating trends in geopotential height anomalies. It is evident based on the two reanalysis datasets. To further inspect the driving force of the ZW3 pattern, we conduct two experiments using the CAM4 model, referring to as SST-SIC-EXP and SIC-EXP (see section 2). In addition, we also employ outputs from the CMIP6 historical run to discuss the possible influence of the external forcing on the ZW3 pattern.

In the SST-SIC-EXP simulation, we first inspect the long-term trend in geopotential height at the 500-hPa level (Fig. 6a). The spatial pattern shows three prominent increasing trend centers, located over northeastern North America, northern Europe, and northeastern Siberia and the North Pacific. The locations of the above centers generally agree with those in the reanalysis, indicating that the model forced with both SST and SIC is capable of reproducing the observed trends in geopotential heights. To better characterize the fluctuations, we zonally decompose the geopotential height field (Fig. 7a) and find that a ZW3 pattern prevails over the other harmonics near 60°N latitude, consistent with the observations. For the 200-hPa level (Fig. 6b), the increasing trends in geopotential height are somewhat agreed with the observations and the decomposed zonal harmonic 3 is still prominent (Fig. 7b). Based on the above analysis, we may conclude that the model simulation that takes both the SST and SIC forcings into account can reproduce

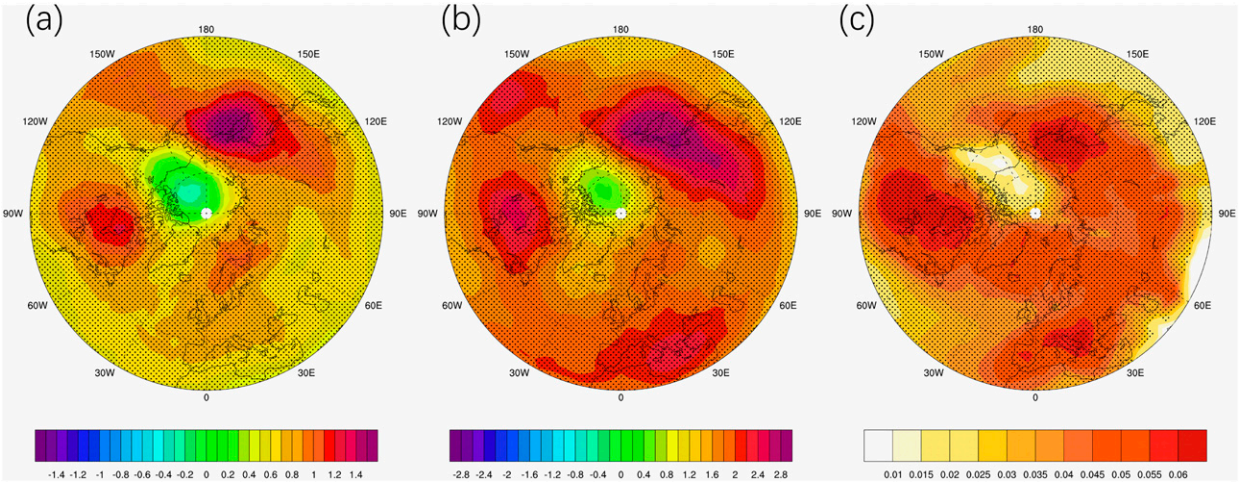

FIG. 6. The long-term trends in (a) 500- and (b) 200-hPa geopotential heights (unit: m yr^{-1}) and (c) 850-hPa air temperature (unit: K yr^{-1}) during the boreal summer in the SST-SIC-EXP. The long-term trend is calculated for the period 1982–2013. The stippling indicates trends that are significant at the 95% confidence level.

the increased trends in geopotential height over the mid- to high latitudes to some extent, forming the observed ZW3 pattern. In comparison with the observation, the long-term trend in 850-hPa air temperature is also inspected in Fig. 6c. The most intense warming centers are located in northeastern North America and northeastern Siberia, consistent with the observed pattern in air temperature (Fig. 3). The decomposed air temperature (Fig. 7c) also suggests that the ZW3 pattern prevails over the other harmonics near 60°N latitude, in accordance with the zonal fluctuations found in upper-level geopotential heights.

We must note that there are inevitable biases that exist between model simulation and observation. The modeled response to the SST forcing is weaker than that observed. The underestimation could be related to the fact that the internal variability is canceled out via a large-ensemble mean and the model deficiency (Scaife and Smith 2018; Suarez-Gutierrez et al. 2021). To quantitatively evaluate the consistency between the modeled and observed patterns, we employ the spatial pattern correlation method, which has been used in previous studies to compare the modeled and observed results (AchutaRao and Sperber 2006; Santer et al. 1996). The correlation coefficient between the 200-hPa trend in SST-SIC-EXP and observation (MERRA data) reaches 0.88. For the trend pattern in 500-hPa geopotential height, the correlation coefficient still reaches 0.64. Other than the geopotential patterns, we also examine the consistency of modeled and observed 850-hPa air temperature (r = 0.78). The above analysis indicates that the SST-SIC-EXP can successfully reproduce the observed patterns to some extent. The key features in the ZW3 pattern are generally consistent.

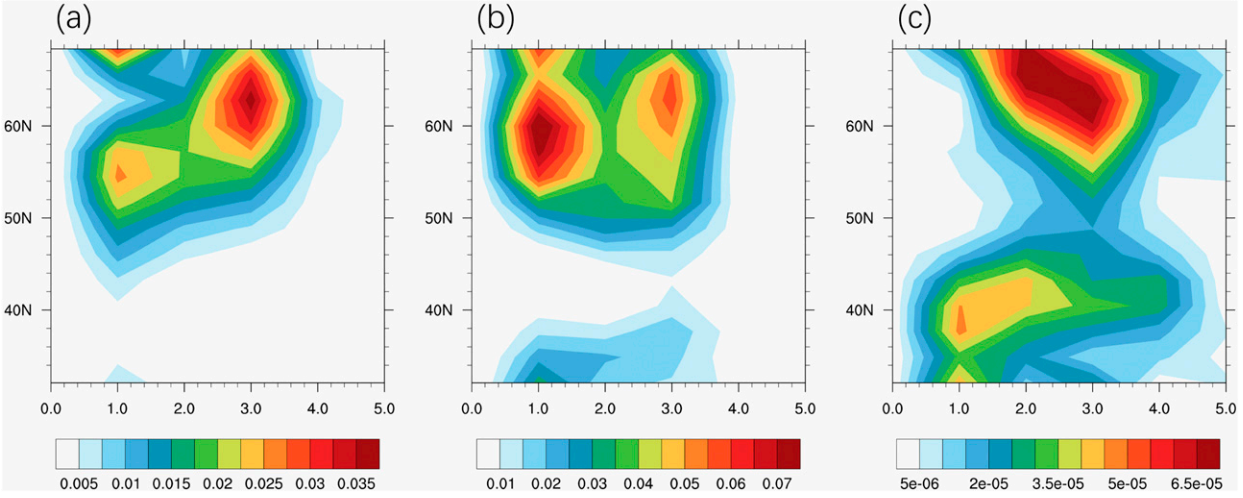

FIG. 7. The amplitude squared of zonal harmonics 1–5 of (a) 500- and (b) 200-hPa geopotential heights (unit: m^2 yr^{-2}), and (c) 850-hPa air temperature (unit: K^2 yr^{-2}) during the boreal summer in the SST-SIC-EXP.

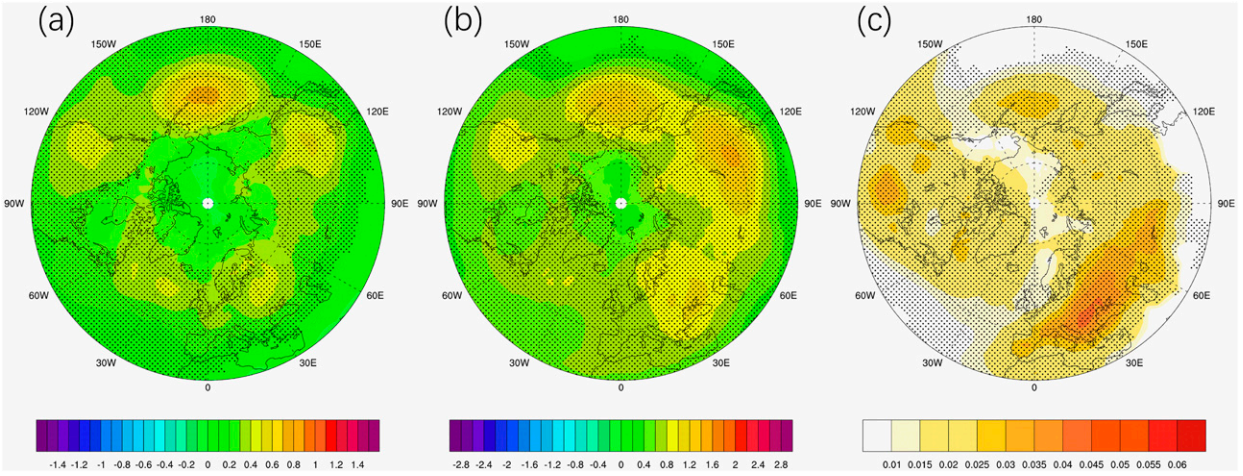

FIG. 8. As in Fig. 6, but for the results obtained from SIC-EXP.

In the SIC-EXP simulation, the trends in geopotential height and air temperature are also examined. Unlike the SST-SIC forced patterns, the experiment without considering the SST forcing gives quite different results. The trends in 500-hPa geopotential height (Fig. 8a) are generally within ± 0.4 m yr^{-1}, with slightly increasing centers located over the North Pacific and the Far East. The trends in northeastern North America, Greenland, Europe, and eastern Siberia are significantly underestimated. Thus, the Arctic sea ice forcing seems very limited in causing the zonal fluctuations in mid- to high-latitude atmospheric circulations. Accordingly, the decomposed zonal harmonics are minor in their amplitudes (Fig. 9a), suggesting that neither the ZW3 trend pattern nor the zonal wave activity can be reproduced with the sea ice-only forcing run. The simulated 200-hPa trend field (Figs. 8b and 9b) is rather weak. The increasing trend in geopotential heights over northeastern North America and Greenland is approximately 3 times smaller than those observed and simulated in the SST-SIC-EXP. Although the trends are significant over the Caspian Sea and Mongolia, the overall trends are weak and insignificant over the mid- to high latitudes. The simulated 850-hPa air temperature (Fig. 8c) shows consistent but rather weak warming trends over the pan-Arctic regions (north of 50°N). Moreover, the warming centers over northeastern North America and Greenland and over eastern Siberia are not as prominent as those in the observations and SST-SIC-EXP. This indicates that the zonal fluctuations of air temperature in the SIC-EXP are very weak so the corresponding zonal harmonics are not significant either (Fig. 9c).

Above all, the decomposed zonal fluctuations in geopotential heights and air temperature in the SST-SIC-EXP and SIC-EXP exhibit consistent zonal wavenumber-1 patterns. Previous studies suggested that the asymmetric responses of land and ocean to the increased radiative forcing intensify the land–sea contrasts (Shaw and Voigt 2015; Sutton et al. 2007) and, therefore, may be responsible for the zonal wavenumber 1.

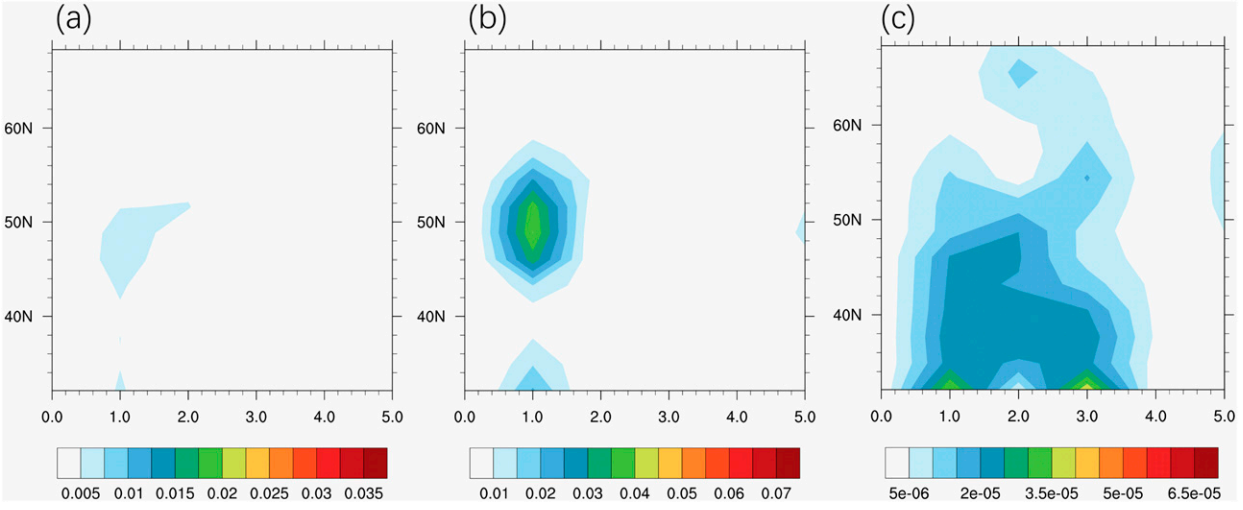

FIG. 9. As in Fig. 7, but for the results obtained from SIC-EXP.

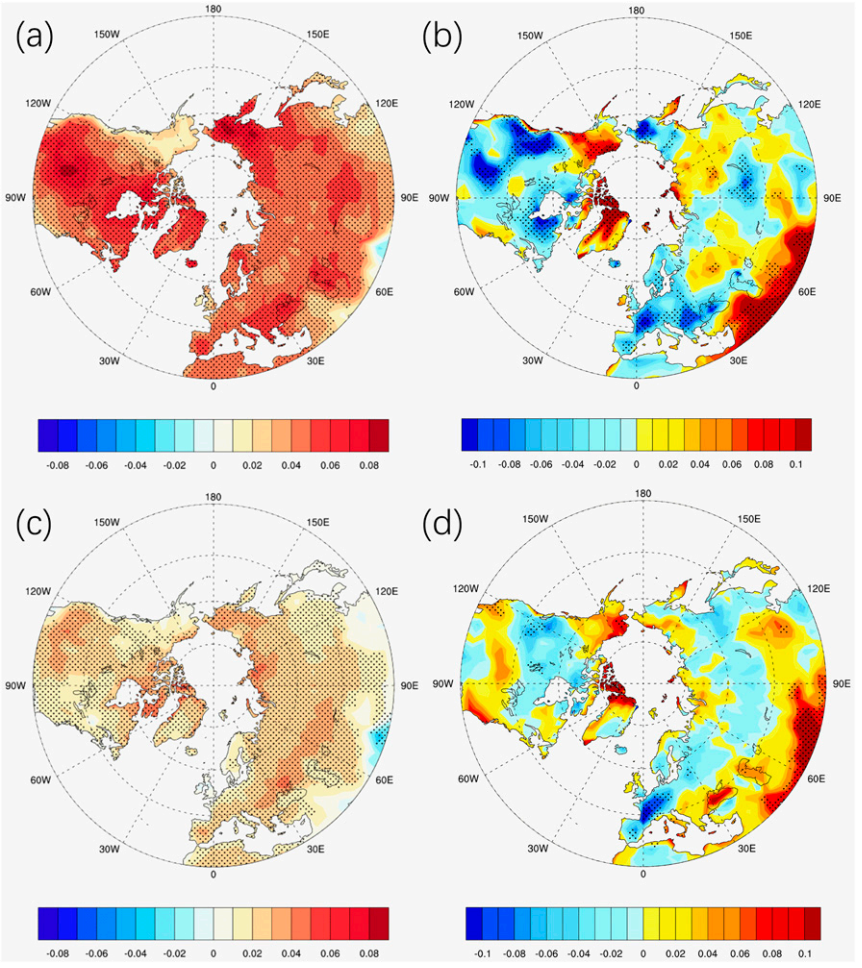

FIG. 10. The long-term trends in summer (a) surface air temperature (unit: K yr^{-1}) and (b) cloudiness (unit: yr^{-1}) in SST-SIC-EXP. (c),(d) As in (a) and (b), but for SIC-EXP. The long-term trend is calculated for the period 1982–2013. The stippling indicates trends that are significant at the 95% confidence level.

We then employ model outputs from the historical experiments in phase 6 of the Coupled Model Intercomparison Project (CMIP6) (see appendix B) in order to examine the responses of atmospheric circulation to the external radiative forcing. The long-term trend in 200-hPa geopotential height in the CMIP6 multimodel ensemble mean (MMEM) (see supplemental Fig. 9a) shows no significant zonal wave train pattern. The simulated zonal gradients of geopotential are weak since the external radiative forcing uniformly affects Earth's surface. However, the responses between ocean and land show slight differences. The geopotential height increased more intense on land over the ocean due to different thermal capacity. We then decompose the externally forced trend pattern (supplemental Fig. 9b). A prominent zonal wavenumber-1 pattern is located near 60°N, while the observed ZW3 pattern barely exists. As discussed above, the effect of external forcing is generally uniform, and the responses of geopotential height mainly differ between land and sea due to contrasting thermal properties. Accordingly, more intense surface warming and increase in geopotential height are found in the Eastern Hemisphere while the response is milder over the Western Hemisphere, resulting in a prominent ZW1 pattern in response to the external radiative forcing. Therefore, we may conclude that the ZW3 is likely dominated by the SST forcing, while the sea ice and external forcing mainly contribute to the formation of ZW1 pattern. Even though the direct influence of the external forcing on ZW3 is limited, it is possible that the external forcing amplifies the forcing role of SST and contributes to the ZW3 to some extent (see section 4).

It has been suggested that the zonal fluctuations in geopotential height can induce synchronized surface warming and cooling trends over mid- to high latitudes, exhibiting a ZW3 pattern. Thus, the simulated SAT trends under the SST-SIC and SIC-only forcing are inspected and compared. The pattern of trends simulated in the SST-SIC-EXP (Fig. 10a) is somewhat consistent with the observation, as the enhanced warming trends are found over the northeastern North America and Greenland region, Europe, Mongolia, and eastern

Siberia. At high-latitude regions, the warming trends correspond with the increased geopotential heights and display a zonal fluctuation to some extent. In general, the warming trends in the Northern Hemisphere are overestimated due to the global warming signal, but the intensity of warming also exhibits regional biases. For example, the warming trends over central North America and northeastern Siberia are larger than observation, while the SATs over northern Europe and Mongolia are underestimated. Nevertheless, the SST-SIC-EXP still captures most of the observed features. It further proves that the upper-level atmospheric fluctuations (the zonal wavenumber-3 pattern) significantly impact the surface warming trends. However, the SAT trends in the SIC-EXP simulation (Fig. 10c) barely agree with the observations. The warming trends over the entire Northern Hemisphere are underestimated. The warming rate is about 2–4 times weaker than that observed in general. Over the mid- to high latitudes, the trends in SAT are small and exhibit no significant zonal difference. In addition, the SAT pattern simulated by CMIP6 MMEM shows strong and zonally uniform warming trends on land, with two significant warming centers located over North America and the Eurasian continent (supplemental Fig. 10). Consistent with the SIC-EXP, the zonal fluctuation is not significant in CMIP6 MMEM either.

As suggested from observational analysis, the SAT is closely related to the upper-level atmospheric circulation. The increase in geopotential heights modifies the regional cloudiness and further changes net surface shortwave radiation, resulting in surface warming and more frequent heatwave activity. In the SST-SIC-EXP (Fig. 10b), the reductions in cloudiness overall correspond with the enhanced warming trends and the increases in geopotential heights. Its spatial pattern exhibits significant zonal fluctuations, with multiple decreasing centers in North America, Europe, and northeastern Siberia. This pattern is somewhat consistent with the observation, except for the large biases are found on the west coast of North America and Greenland, suggesting that the cloud-radiation feedback can explain the SAT warming to some extent, but uncertainty remains in the model simulation. However, the decreasing trend in cloudiness is not prominent over the mid- to high latitudes in the SIC-EXP (Fig. 10d) due to the weak geopotential heights increase under the sea ice forcing alone. In Europe, it shows a significant decline, but the zonal difference is minor across the Eurasian continent. Thus, the trends in SAT show no zonal fluctuation accordingly. The difference of simulated cloudiness between the SST-SIC-EXP and SIC-EXP highlights the vital role of clouds in causing the surface warming trends and linking them with the zonal fluctuations in atmospheric circulation.

Comparing results in the SST-SIC-EXP with the SIC-EXP indicates that the Arctic sea ice and the associated external forcing have minimal influence on the ZW3 pattern in geopotential heights. Thus, it can hardly explain the observed warming trends and their interconnections via the cloud-shortwave radiation process. By contrast, the simulation with the SST forcing involved can reproduce the overall warming trends in the Northern Hemisphere continents. It provides model evidence that the Northern Hemisphere hotspots are closely connected with the SST forcing other than the Arctic sea ice. More importantly, these hotspots may be interconnected through SST-excited wave trains, exhibiting a ZW3 pattern in geopotential height and SAT along 60°N latitude.

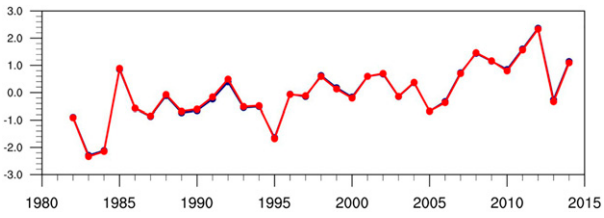

FIG. 11. The time series of the normalized zonal wavenumber-3 index using MERRA (red line) and JRA-55 (blue line) for the period 1982–2014.

c. *Zonal wave patterns perturbed by subtropical SSTs*

Based on the above analysis, the ZW3 pattern linking the Northern Hemisphere hotspots is likely excited by the SST since the zonal fluctuations are significant only when the SST forcing has been prescribed the model. Here, we define the zonal wavenumber-3 index by summarizing the geopotential heights of each active center (Fig. 1). The normalized index is displayed for the period 1982–2014 using MERRA and JRA-55 data. The two datasets exhibit a consistently increasing trend, and the interannual variabilities are very consistent (Fig. 11). We then calculate the correlation between the Northern Hemisphere SSTs and the index to determine which part of the oceans is related to the ZW3 pattern in geopotential heights. In Fig. 12, the results obtained from the two datasets are very close. Both of them indicate strong correlations of the ZW3 pattern with the subtropical SSTs. For instance, the western North Pacific and subtropical North Atlantic exhibit quite prominent warming, as the correlation coefficients are larger than 0.5. Also, there is relatively weak SST warming in the eastern North Pacific. These significant warming zones are likely the heat sources that excite the zonal wave train over the mid- to high latitudes. Note that the northern North Pacific SST is also positively correlated with the zonal wave train. However, the North Pacific SST is likely to be a consequence of the wave train rather than a cause (Amaya et al. 2020; Johnstone and Mantua 2014). This is because the atmospheric circulation normally forces the mid- to high-latitude SSTs, and the North Pacific region is governed by a strong high pressure anomaly, corresponding to the positive phase of the wave train.

It is known that the tropical (subtropical) heat sources are able to excite the Rossby wave train, propagating along the great circle path and influencing the mid- to high-latitude atmospheric circulations (Hoskins and Karoly 1981). It is suggested that the atmospheric response near the tropical heat source is baroclinic, but the remote atmospheric response to the heat source is equivalent barotropic since the baroclinic Rossby wave is often confined to the tropics (Kosaka and Nakamura 2006). The summer ZW3 patterns in the

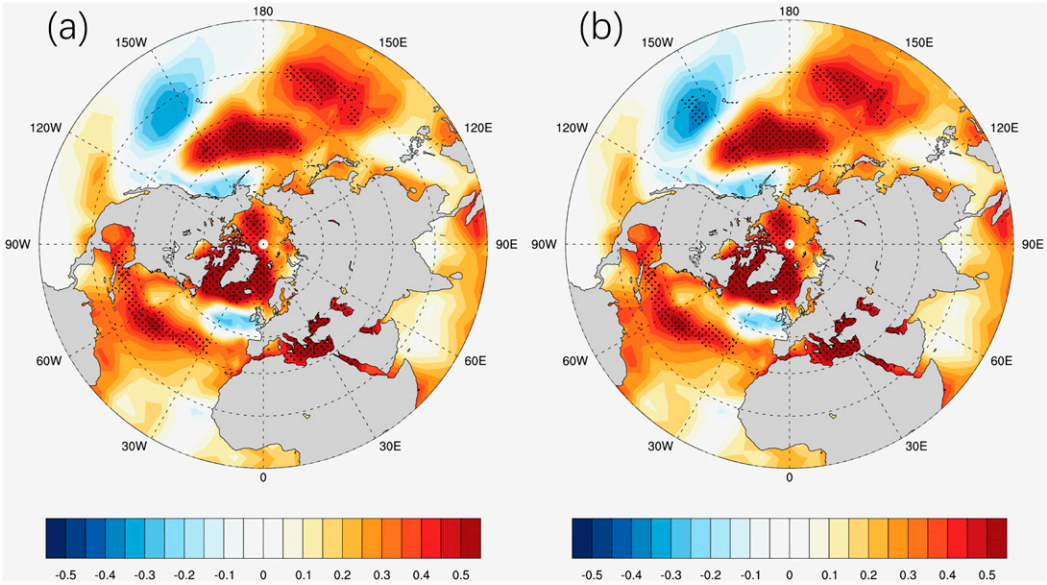

FIG. 12. The correlation pattern between the zonal wavenumber-3 index and the Northern Hemisphere SSTs. The index is derived based on the (a) MERRA and (b) JRA-55 datasets.

observations and SST-SIC-EXP ACGM experiments are of large scale and equivalent-barotropic. It is expected that a nondivergent barotropic vorticity equation model can capture the main dynamical features of the ZW3 pattern. Previous studies have suggested that the linear barotropic model is useful in interpreting observational and AGCM responses to SST anomalies (Branstator 1985a,b; Ting 1996). Branstator applied such a simple linear model to reproduce the midlatitude atmospheric responses to Pacific SST anomalies and compared them to the AGCM results. It is suggested that the barotropic model can reproduce the structure of the pattern to some extent if it is forced by a vorticity source/sink in approximately the same geographical location as the SST anomaly (Branstator 1985a,b). Moreover, when a barotropic model is applied at the barotropic equivalent level, it can reproduce the extratropical atmospheric response as effectively as the baroclinic model does (Ting 1996). Therefore, we employ a theoretical barotropic model to investigate the extratropical response to specific lower-latitude SST heating, which acts as a vorticity source/sink in the barotropic vorticity equation. According to the correlation maps between the ZW3 index and SST (Fig. 12), we select three centers located in subtropical North Atlantic (28°N, 57°W), eastern North Pacific (18°N, 140°W), and western North Pacific (15°N, 160°E) as vorticity sources/sinks in the linear barotropic model, in order to determine the possible origin of the ZW3. The results are given as follows.

Subtropical North Atlantic: In Fig. 13a, a Rossby wave train is excited from the subtropical North Atlantic near the Gulf region, propagating across the North Atlantic and extending toward the Far East region with alternating high and low geopotential anomalies. The upper-level troposphere near the heat source shows a pressure decline due to the diabetic heating of the underlying ocean. When the Rossby wave train propagates into the mid- to high latitudes, the spatial pattern resembles the observed trends in geopotential heights (Fig. 1). For instance, northeastern North America, Europe, and northeastern Siberia are governed by high geopotential anomalies, while the northeastern North Atlantic and central Siberia exhibit a significant decline in geopotential heights, generally consistent with the observed ZW3 pattern. Thus, the barotropic model with a heat source over the subtropical North Atlantic can reproduce some of the key features in the observed wave trains, indicating that the North Atlantic SST plays an important role in forming the ZW3 pattern in the North Hemisphere mid- to high latitudes.

Eastern North Pacific: The extratropical atmospheric response to the eastern North Pacific heat source also shows a wave train pattern (Fig. 13b). Consistently, an increase in geopotential heights is found in the northeastern North America and Greenland region, Europe, and eastern Siberia, agreeing with the observation. However, the overall intensity of this wave train is rather weak, and no significant activity center can be recognized. As suggested in previous studies (Wallace and Lau 1985), the barotropic energy is easily converted over the jet regions to feed the development of the wave train. Since the heat source is far from the jet regions, the excited wave train is unlikely to obtain barotropic energy from the basic flow. Therefore, the eastern North Pacific SST contribution to the zonal wave train pattern is minimal.

Western North Pacific: The western North Pacific region has the world's largest warm pool, preserving a considerable amount of energy in the ocean. Since the SST in this region exhibits a significant correlation with the zonal wavenumber-3 index, it is essential to examine the atmospheric

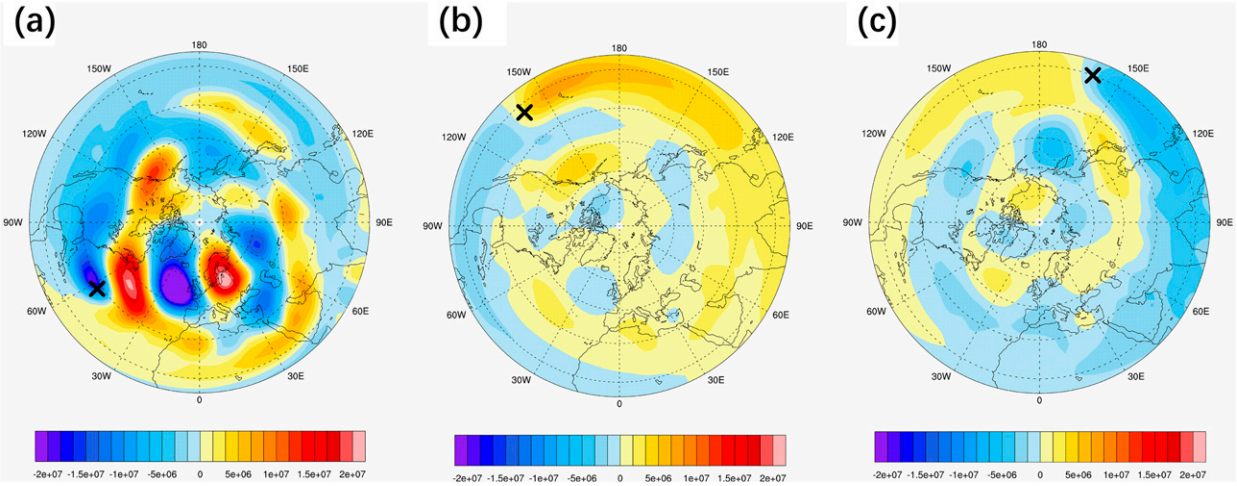

FIG. 13. The 500-hPa atmospheric horizontal streamfunction (units: $m^2\ s^{-1}$) simulated by the theoretical barotropic model in response to the vorticity source/sink centered over the (a) subtropical North Atlantic (28°N, 57°W), (b) eastern North Pacific (18°N, 140°W), and (c) western North Pacific (15°N, 160°E), which have been marked with a black cross in each panel.

response to the western North Pacific heat source. As shown in Fig. 13c, the heat source excites a Rossby wave train over the extratropical regions, and the spatial pattern notably resembles the Pacific–Japan (PJ) pattern (Nitta 1987, 1989). There is a low pressure anomaly over the western North Pacific region in response to the diabatic heating, accompanied by the following high and low pressure anomalies alternatively distributed over the North Pacific Ocean, showing a meridionally propagating structure. This meridional wave train pattern disagrees with the observed ZW3 pattern, as responses over the North Atlantic and Eurasian continent are too weak, and there is noticeable disagreement over eastern Siberia.

Based on the above analysis, we find that the tropical heat sources over the western and eastern North Pacific can only excite weak extratropical atmospheric responses in the barotropic model, and the wave train patterns barely match the observed ones. By contrast, the atmospheric circulation forced by the subtropical North Atlantic heating exhibits a strong zonal wave train pattern, which resembles the observed one. We further conduct an experiment using a state-of-the-art AGCM forced by the observed monthly varying SST over the Atlantic basin, and the climatological monthly SSTs are prescribed in the Indo-Pacific region, referred to as SST-ATL-EXP (see appendix C). In the SST-ATL-EXP, the trend pattern of 200-hPa geopotential height shows a Rossby wave train along 60°N latitude, exhibiting a ZW3 pattern (supplemental Fig. 11a). The simulated pattern is consistent with the observation, which consists of three centers of action located over the North Atlantic, eastern Europe, and eastern Siberia. The simulated trend patterns in SST-ATL-EXP and SST-SIC-EXP are compared via spatial correlation. The correlation coefficient reaches 0.83, indicating that the coherence between the observation and SST-SIC-EXP may be mainly explained by the North Atlantic signal. We further inspect the responses of surface air temperature (SAT) in SST-ATL-EXP (supplemental Fig. 11b), and the simulated pattern is overall consistent with the observation. The AGCM forced by the North Atlantic SST can successfully reproduce the observed ZW3 pattern in upper-level geopotential height and the associated surface warming. In addition to the theoretical model, SST-ATL-EXP highlights the importance of the North Atlantic SST, further suggesting that the North Atlantic SST is mainly responsible for the ZW3 pattern.

4. Discussion

We calculate the theoretical stationary wavenumber (see appendix D) to discuss why the ZW3 is preferred over other harmonics (supplemental Fig. 12). The wavenumber-3 bands are found near 60° latitude in both the Southern and Northern Hemispheres, consistent with the prominent amplitude of zonal harmonic 3 and the existence of zonally propagating zonal wavenumber 3 within these latitudes (55°–70°N) in both observations and model simulations. It indicates that the ZW3 is likely an intrinsic mode of atmospheric circulation, supported by basic Rossby wave propagation theories. According to the calculation of stationary wavenumber (see the supplemental material), the intensity of zonal wind determines the theoretical limits of zonal wavenumber for zonal waves. Therefore, the westerly basic flow may be critical to the formation of the ZW3 pattern. In addition, a previous study also suggested that the interaction with synoptic eddies may contribute to the ZW3 pattern (Teng and Branstator 2012). Other than the aforementioned two possible mechanisms, more thorough analyzes should be carried out in future work to better understand the characteristics of the ZW3 pattern using more sophisticated numerical models.

In this study, the subtropical North Atlantic SST thought to excite the ZW3 pattern has strong variabilities, such as the

Atlantic multidecadal oscillation (AMO). The driving force of the North Atlantic SST variability is still under debate. Some previous studies pointed out that the AMO is mainly driven by internal forcings (Zhang et al. 2019), whereas others suggested that the external forcing contributes significantly to the AMO (Qin et al. 2020). However, in this study, the ZW3 pattern cannot be reproduced by the CMIP6 MMEM (supplemental Fig. 9), indicating that the direct influence of external forcing on the ZW3 is limited. The responses of geopotential height to the external forcing mainly differ between land and sea due to contrasting thermal properties, exhibiting a prominent zonal wavenumber-1 pattern. Nevertheless, the contribution of external forcing cannot be completely ruled out. The externally forced component of the North Atlantic SST may contribute to the ZW3 to some extent. Thus, future work needs to inspect the relative roles of the internal and external components of the North Atlantic SST in modulating the ZW3 pattern.

5. Conclusions

In this study, we identify a ZW3 pattern in the trends of tropospheric atmospheric circulation during the recent decades. The ZW3 is mainly confined within the mid- to high latitudes, especially near 60°N. The ZW3 patterns are found prominent at both 500 and 200 hPa, indicating a barotropic structure. The wave train pattern consists of multiple increasing trend centers, which are located in northeastern North America and Greenland, Europe, and eastern Siberia. Through wave flux analysis, we find strong interconnectivity among these centers, indicating an eastward wave energy dispersion. In addition, these regions with strong increasing trends in geopotential heights also exhibit enhanced surface warming trends. Further analysis suggests that the increased geopotential heights reduce cloudiness and increase net surface shortwave radiation, resulting in strong SAT warming and an associated increase in heatwave amplitude and frequency. Therefore, the summertime zonal wavenumber-3 pattern gives a new insight into the interconnections among these warming trends and regards them as a part of the intrinsic zonal fluctuations in the atmospheric circulation.

To determine the driving force of the ZW3 pattern, we conduct a series of model simulations, including SST-SIC-EXP, SIC-EXP, and CMIP6 MMEM. The experiment with the global SST prescribed in the model can successfully reproduce the observed zonal wave train pattern, while the model forced by the sea ice cannot reproduce the ZW3 pattern. Moreover, the external radiative forcing is mainly responsible for a zonal wavenumber-1 pattern, while the ZW3 is not significant in CMIP6 MMEM. Thus, we can conclude that the SST forcing is likely a key factor in the formation of the observed ZW3 pattern. Furthermore, we find that the subtropical North Atlantic SST can excite a zonal wave train that resembles the observed ZW3 pattern in both theoretical barotropic model and state-of-the-art AGCM (SST-ATL-EXP). This study demonstrates a ZW3 pattern in the mid- to high-latitude atmospheric circulation and highlights its role in modulating the mean surface air temperature as well as heatwaves. It provides evidence that the observed Northern Hemisphere hotspots may be interconnected via the upper-level atmospheric zonal wave train.

Acknowledgments. The authors wish to thank the three anonymous reviewers for their constructive comments that significantly improved the quality of this paper. This work was jointly supported by the National Natural Science Foundation of China (41775038, 41790474 and 41975082), Shandong Natural Science Foundation Project (ZR2019ZD12), and the National Programme on Global Change and Air–Sea Interaction (GASI-IPOVAI-06 and GASI-IPOVAI-03).

Data availability statement. All data that support the findings of this study are included within the article (and any supplemental files).

APPENDIX A

Wave Activity Flux

Wave flux analysis is carried out to examine the underlying physics of Rossby wave energy propagation. Since the wave activity flux (**F**) is parallel to the group velocity of stationary Rossby waves, it indicates the source and propagation direction of stationary Rossby waves. The wave activity flux is computed following the method proposed by Plumb (1985):

$$F_\lambda = p \times \frac{1}{2a^2\cos\phi}\left[\left(\frac{\partial\psi'}{\partial\lambda}\right)^2 - \psi'\frac{\partial^2\psi'}{\partial\lambda^2}\right],$$

$$F_\phi = p \times \frac{1}{2a^2}\left(\frac{\partial\psi'}{\partial\lambda}\frac{\partial\psi'}{\partial\phi} - \psi'\frac{\partial^2\psi'}{\partial\lambda\partial\phi}\right),$$

where p is pressure/1000 hPa, a is Earth's radius, and ψ is the streamfunction; ϕ and λ indicate latitude and longitude, respectively. The wave activity flux is calculated based on 200- and 500-hPa geopotential heights derived from the JRA-55 dataset.

APPENDIX B

CMIP6 Historical Experiment

To identify the response of upper-level atmospheric circulation to the external radiative forcing, we employ model outputs from phase 6 of the Coupled Model Intercomparison Project (CMIP6) (Eyring et al. 2016). We use fully coupled models from the CMIP6 historical experiment, with a total of 50 ensemble members from 32 CMIP6 models (supplemental Table 1). The external forcing and forced signal in each ensemble member are consistent. Via the multimodel ensemble mean (MMEM), the internal variability in different runs is uncorrelated and canceled out, considering the large ensemble size. Therefore, the externally forced component of climate

variability in response to the time-varying radiative forcing can be reasonably represented by the CMIP6 MMEM.

APPENDIX C

SST-ATL-EXP

The SST-ATL-EXP is conducted using a state-of-the-art AGCM developed by the International Centre of Theoretical Physics (ICTP AGCM, version 41) (Kucharski et al. 2016). The AGCM is forced by the observed monthly varying SST over the Atlantic basin and the climatological monthly SSTs are prescribed in the Indo-Pacific region. This experiment aims to directly assess the impact of SST forcing on the atmospheric circulation and to highlight the contributions from the North Atlantic Ocean. Details about the experimental configurations of the SST-ATL-EXP simulation are given in Kucharski et al. (2016). The SST-ATL-EXP simulation has five ensemble members, which are all transient runs. The results of the ensemble members are averaged and analyzed for the period 1982–2013.

APPENDIX D

Theoretical Zonal Wavenumber

The theoretical stationary wavenumber in a fixed basic flow U is calculated based on the method in Hoskins and Ambrizzi (1993):

$$K = \sqrt{k^2 + l^2}$$

is the total wavenumber, where k and l indicate the zonal and meridional wavenumbers, respectively.

$$K = \cos\phi \sqrt{\frac{\left[2\Omega - \left(\frac{1}{\cos\phi}\frac{\partial}{\partial\phi}\right)^2 (\cos^2\phi\bar{v})\right]}{\bar{v}}},$$

where ϕ is the latitude, Ω is Earth's rotation rate, and $\bar{v} = \bar{U}/a\cos\phi$ is the relative rotation rate of the atmosphere. The stationary wavenumber is calculated based on the long-term climatology of the zonal-mean zonal wind at 200 and 500 hPa during the boreal summer. From the definition, the stationary wavenumber (K) corresponds to the theoretical upper limit for stationary zonal wavenumber k and equals k when the meridional wave propagation is negligible.

REFERENCES

AchutaRao, K., and K. R. Sperber, 2006: ENSO simulation in coupled ocean–atmosphere models: Are the current models better? *Climate Dyn.*, **27** (1), 1–15, https://doi.org/10.1007/s00382-006-0119-7.

Amaya, D. J., A. J. Miller, S.-P. Xie, and Y. Kosaka, 2020: Physical drivers of the summer 2019 North Pacific marine heatwave. *Nat. Commun.*, **11**, 1903, https://doi.org/10.1038/s41467-020-15820-w.

Boé, J., and Coauthors, 2020: Past long-term summer warming over Western Europe in new generation climate models: Role of large-scale atmospheric circulation. *Environ. Res. Lett.*, **15**, 084038, https://doi.org/10.1088/1748-9326/ab8a89.

Branstator, G., 1985a: Analysis of general circulation model sea surface temperature anomaly simulations using a linear model. Part I: Forced solutions. *J. Atmos. Sci.*, **42**, 2225–2241, https://doi.org/10.1175/1520-0469(1985)042<2225:AOGCMS>2.0.CO;2.

——, 1985b: Analysis of general-circulation model sea surface temperature anomaly simulations using a linear-model. Part II: Eigenanalysis. *J. Atmos. Sci.*, **42**, 2242–2254, https://doi.org/10.1175/1520-0469(1985)042<2242:AOGCMS>2.0.CO;2.

Budikova, D., T. W. Ford, and T. J. Ballinger, 2017: Connections between North-Central United States summer hydroclimatology and Arctic sea ice variability. *Int. J. Climatol.*, **37**, 4434–4450, https://doi.org/10.1002/joc.5097.

Cai, Q. Q., J. Wang, D. Beletsky, J. Overland, M. Ikeda, and L. Y. Wan, 2021: Accelerated decline of summer Arctic sea ice during 1850–2017 and the amplified Arctic warming during the recent decades. *Environ. Res. Lett.*, **16**, 8, https://doi.org/10.1088/1748-9326/abdb5f.

Cassou, C., L. Terray, and A. S. Phillips, 2005: Tropical Atlantic influence on European heat waves. *J. Climate*, **18**, 2805–2811, https://doi.org/10.1175/JCLI3506.1.

Cavalieri, D. J., C. L. Parkinson, P. Gloersen, and H. J. Zwally, 1996: Sea ice concentrations from Nimbus-7 SMMR and DMSP SSM/ISSMIS passive microwave data. NASA National Snow and Ice Data Center Distributed Active Archive Center, accessed 2021, https://doi.org/10.5067/8GQ8LZQVL0VL.

Chen, H., B. Yu, B. Zhou, W. Zhang, and J. Zhang, 2020: Role of local atmospheric forcing and land–atmosphere interaction in recent land surface warming in the midlatitudes over East Asia. *J. Climate*, **33**, 2295–2309, https://doi.org/10.1175/JCLI-D-18-0856.1.

Christidis, N., P. A. Stott, S. Brown, G. C. Hegerl, and J. Caesar, 2005: Detection of changes in temperature extremes during the second half of the 20th century. *Geophys. Res. Lett.*, **32**, L20716, https://doi.org/10.1029/2005GL023885.

Cohen, J., and Coauthors, 2014: Recent Arctic amplification and extreme mid-latitude weather. *Nat. Geosci.*, **7**, 627–637, https://doi.org/10.1038/ngeo2234.

Compo, G. P., and P. D. Sardeshmukh, 2009: Oceanic influences on recent continental warming. *Climate Dyn.*, **32**, 333–342, https://doi.org/10.1007/s00382-008-0448-9.

Coumou, D., V. Petoukhov, S. Rahmstorf, S. Petri, and H. J. Schellnhuber, 2014: Quasi-resonant circulation regimes and hemispheric synchronization of extreme weather in boreal summer. *Proc. Natl. Acad. Sci. USA*, **111**, 12 331–12 336, https://doi.org/10.1073/pnas.1412797111.

——, G. Di Capua, S. Vavrus, L. Wang, and S. Wang, 2018: The influence of Arctic amplification on mid-latitude summer circulation. *Nat. Commun.*, **9**, 12, https://doi.org/10.1038/s41467-018-05256-8.

Della-Marta, P. M., J. Luterbacher, H. von Weissenfluh, E. Xoplaki, M. Brunet, and H. Wanner, 2007: Summer heat waves over western Europe 1880–2003, their relationship to large-scale forcings and predictability. *Climate Dyn.*, **29**, 251–275, https://doi.org/10.1007/s00382-007-0233-1.

Ding, Q., and B. Wang, 2005: Circumglobal teleconnection in the Northern Hemisphere summer. *J. Climate*, **18**, 3483–3505, https://doi.org/10.1175/JCLI3473.1.

Dong, B., R. T. Sutton, and L. Shaffrey, 2017: Understanding the rapid summer warming and changes in temperature extremes

since the mid-1990s over Western Europe. *Climate Dyn.*, **48**, 1537–1554, https://doi.org/10.1007/s00382-016-3158-8.

Dosio, A., L. Mentaschi, E. M. Fischer, and K. Wyser, 2018: Extreme heat waves under 1.5°C and 2°C global warming. *Environ. Res. Lett.*, **13**, 10, https://doi.org/10.1088/1748-9326/aab827.

Eyring, V., S. Bony, G. A. Meehl, C. A. Senior, B. Stevens, R. J. Stouffer, and K. E. Taylor, 2016: Overview of the Coupled Model Intercomparison Project Phase 6 (CMIP6) experimental design and organization. *Geosci. Model Dev.*, **9**, 1937–1958, https://doi.org/10.5194/gmd-9-1937-2016.

Field, C. B., and Coauthors, Eds., 2012: *Managing the Risks of Extreme Events and Disasters to Advance Climate Change Adaptation.* Cambridge University Press, 582 pp.

Fischer, E. M., and C. Schar, 2009: Future changes in daily summer temperature variability: Driving processes and role for temperature extremes. *Climate Dyn.*, **33**, 917–935, https://doi.org/10.1007/s00382-008-0473-8.

——, and ——, 2010: Consistent geographical patterns of changes in high-impact European heatwaves. *Nat. Geosci.*, **3**, 398–403, https://doi.org/10.1038/ngeo866.

——, S. I. Seneviratne, D. Luthi, and C. Schar, 2007a: Contribution of land–atmosphere coupling to recent European summer heat waves. *Geophys. Res. Lett.*, **34**, L06707, https://doi.org/10.1029/2006GL029068.

——, ——, P. L. Vidale, D. Luthi, and C. Schar, 2007b: Soil moisture–atmosphere interactions during the 2003 European summer heat wave. *J. Climate*, **20**, 5081–5099, https://doi.org/10.1175/JCLI4288.1.

Gao, M., J. Yang, D. Gong, P. Shi, Z. Han, and S.-J. Kim, 2019: Footprints of Atlantic multidecadal oscillation in the low-frequency variation of extreme high temperature in the Northern Hemisphere. *J. Climate*, **32**, 791–802, https://doi.org/10.1175/JCLI-D-18-0446.1.

Grumbine, R. W., 1996: Automated passive microwave sea ice concentration analysis at NCEP. NCEP/NWS/NOAA Tech. Note, OMB Contribution 120, 13 pp., https://polar.ncep.noaa.gov/mmab/papers/tn120/ssmi120.pdf.

Hartmann, D., and Coauthors, 2013: Observations: Atmosphere and surface. *Climate Change 2013: The Physical Science Basis*, T. F. Stocker et al., Eds., Cambridge University Press, 159–254.

Hersbach, H., and Coauthors, 2020: The ERA5 global reanalysis. *Quart. J. Roy. Meteor. Soc.*, **146**, 1999–2049, https://doi.org/10.1002/qj.3803.

Hong, X., R. Lu, and S. Li, 2017: Amplified summer warming in Europe–West Asia and Northeast Asia after the mid-1990s. *Environ. Res. Lett.*, **12**, 094007, https://doi.org/10.1088/1748-9326/aa7909.

Horton, D. E., N. C. Johnson, D. Singh, D. L. Swain, B. Rajaratnam, and N. S. Diffenbaugh, 2015: Contribution of changes in atmospheric circulation patterns to extreme temperature trends. *Nature*, **522**, 465–469, https://doi.org/10.1038/nature14550.

Hoskins, B. J., and D. J. Karoly, 1981: The steady linear response of a spherical atmosphere to thermal and orographic forcing. *J. Atmos. Sci.*, **38**, 1179–1196, https://doi.org/10.1175/1520-0469(1981)038<1179:TSLROA>2.0.CO;2.

——, and T. Ambrizzi, 1993: Rossby wave propagation on a realistic longitudinally varying flow. *J. Atmos. Sci.*, **50**, 1661–1671, https://doi.org/10.1175/1520-0469(1993)050<1661:RWPOAR>2.0.CO;2.

Hsu, P.-C., Y. Qian, Y. Liu, H. Murakami, and Y. Gao, 2020: Role of abnormally enhanced MJO over the western Pacific in the formation and subseasonal predictability of the record-breaking Northeast Asian heatwave in the summer of 2018. *J. Climate*, **33**, 3333–3349, https://doi.org/10.1175/JCLI-D-19-0337.1.

Hu, K., G. Huang, and R. Huang, 2011: The impact of tropical Indian Ocean variability on summer surface air temperature in China. *J. Climate*, **24**, 5365–5377, https://doi.org/10.1175/2011JCLI4152.1.

Huang, B., and Coauthors, 2017: Extended reconstructed sea surface temperature, version 5 (ERSSTv5): Upgrades, validations, and intercomparisons. *J. Climate*, **30**, 8179–8205, https://doi.org/10.1175/JCLI-D-16-0836.1.

Johnstone, J. A., and N. J. Mantua, 2014: Atmospheric controls on northeast Pacific temperature variability and change, 1900–2012. *Proc. Natl. Acad. Sci. USA*, **111**, 14 360–14 365, https://doi.org/10.1073/pnas.1318371111.

Klein Tank, A., and G. Können, 2003: Trends in indices of daily temperature and precipitation extremes in Europe, 1946–99. *J. Climate*, **16**, 3665–3680, https://doi.org/10.1175/1520-0442(2003)016<3665:TIIODT>2.0.CO;2.

Kobayashi, S., and Coauthors, 2015: The JRA-55 reanalysis: General specifications and basic characteristics. *J. Meteor. Soc. Japan*, **93**, 5–48, https://doi.org/10.2151/jmsj.2015-001.

Kornhuber, K., V. Petoukhov, S. Petri, S. Rahmstorf, and D. Coumou, 2017a: Evidence for wave resonance as a key mechanism for generating high-amplitude quasi-stationary waves in boreal summer. *Climate Dyn.*, **49**, 1961–1979, https://doi.org/10.1007/s00382-016-3399-6.

——, ——, D. Karoly, S. Petri, S. Rahmstorf, and D. Coumou, 2017b: Summertime planetary wave resonance in the Northern and Southern Hemispheres. *J. Climate*, **30**, 6133–6150, https://doi.org/10.1175/JCLI-D-16-0703.1.

——, S. Osprey, D. Coumou, S. Petri, V. Petoukhov, S. Rahmstorf, and L. Gray, 2019: Extreme weather events in early summer 2018 connected by a recurrent hemispheric wave-7 pattern. *Environ. Res. Lett.*, **14**, 054002, https://doi.org/10.1088/1748-9326/ab13bf.

Kosaka, Y., and H. Nakamura, 2006: Structure and dynamics of the summertime Pacific–Japan teleconnection pattern. *Quart. J. Roy. Meteor. Soc.*, **132**, 2009–2030, https://doi.org/10.1256/qj.05.204.

Kucharski, F., and Coauthors, 2016: The teleconnection of the tropical Atlantic to Indo-Pacific sea surface temperatures on inter-annual to centennial time scales: A review of recent findings. *Atmosphere*, **7**, 29, https://doi.org/10.3390/atmos7020029.

Kysely, J., 2007: Implications of enhanced persistence of atmospheric circulation for the occurrence and severity of temperature extremes. *Int. J. Climatol.*, **27**, 689–695, https://doi.org/10.1002/joc.1478.

——, and P. Domonkos, 2006: Recent increase in persistence of atmospheric circulation over Europe: Comparison with long-term variations since 1881. *Int. J. Climatol.*, **26**, 461–483, https://doi.org/10.1002/joc.1265.

Meehl, G. A., and C. Tebaldi, 2004: More intense, more frequent, and longer lasting heat waves in the 21st century. *Science*, **305**, 994–997, https://doi.org/10.1126/science.1098704.

Morice, C. P., J. J. Kennedy, N. A. Rayner, and P. D. Jones, 2012: Quantifying uncertainties in global and regional temperature change using an ensemble of observational estimates: The HadCRUT4 data set. *J. Geophys. Res.*, **117**, D08101, https://doi.org/10.1029/2011JD017187.

Neale, R. B., J. Richter, S. Park, P. H. Lauritzen, S. J. Vavrus, P. J. Rasch, and M. Zhang, 2013: The mean climate of the

Community Atmosphere Model (CAM4) in forced SST and fully coupled experiments. *J. Climate*, **26**, 5150–5168, https://doi.org/10.1175/JCLI-D-12-00236.1.

Nitta, T., 1987: Convective activities in the tropical western Pacific and their impact on the Northern Hemisphere summer circulation. *J. Meteor. Soc. Japan*, **65**, 373–390, https://doi.org/10.2151/jmsj1965.65.3_373.

——, 1989: Global features of the Pacific-Japan oscillation. *Meteor. Atmos. Phys.*, **41**, 5–12, https://doi.org/10.1007/BF01032585.

Ogawa, F., and Coauthors, 2018: Evaluating impacts of recent Arctic sea ice loss on the Northern Hemisphere winter climate change. *Geophys. Res. Lett.*, **45**, 3255–3263, https://doi.org/10.1002/2017GL076502.

Overland, J. E., and M. Y. Wang, 2010: Large-scale atmospheric circulation changes are associated with the recent loss of Arctic sea ice. *Tellus*, **62A** (1), 1–9, https://doi.org/10.1111/j.1600-0870.2009.00421.x.

Perkins, S. E., 2015: A review on the scientific understanding of heatwaves—Their measurement, driving mechanisms, and changes at the global scale. *Atmos. Res.*, **164**, 242–267, https://doi.org/10.1016/j.atmosres.2015.05.014.

——, and L. V. Alexander, 2013: On the measurement of heat waves. *J. Climate*, **26**, 4500–4517, https://doi.org/10.1175/JCLI-D-12-00383.1.

Perkins-Kirkpatrick, S. E., and S. Lewis, 2020: Increasing trends in regional heatwaves. *Nat. Commun.*, **11**, 3357, https://doi.org/10.1038/s41467-020-16970-7.

——, E. M. Fischer, O. Angélil, and P. B. Gibson, 2017: The influence of internal climate variability on heatwave frequency trends. *Environ. Res. Lett.*, **12**, 044005, https://doi.org/10.1088/1748-9326/aa63fe.

Plumb, R. A., 1985: On the three-dimensional propagation of stationary waves. *J. Atmos. Sci.*, **42**, 217–229, https://doi.org/10.1175/1520-0469(1985)042<0217:OTTDPO>2.0.CO;2.

Qian, Y. T., H. Murakami, P. C. Hsu, and S. B. Kapnick, 2020: Effects of anthropogenic forcing and natural variability on the 2018 heatwave in Northeast Asia. *Bull. Amer. Meteor. Soc.*, **101**, S77–S82, https://doi.org/10.1175/BAMS-D-19-0156.1.

Qin, M., A. Dai, and W. Hua, 2020: Aerosol-forced multidecadal variations across all ocean basins in models and observations since 1920. *Sci. Adv.*, **6**, eabb0425, https://doi.org/10.1126/sciadv.abb0425.

Reynolds, R. W., T. M. Smith, C. Liu, D. B. Chelton, K. S. Casey, and M. G. Schlax, 2007: Daily high-resolution-blended analyses for sea surface temperature. *J. Climate*, **20**, 5473–5496, https://doi.org/10.1175/2007JCLI1824.1.

Rienecker, M. M., and Coauthors, 2011: MERRA: NASA's Modern-Era Retrospective Analysis for Research and Applications. *J. Climate*, **24**, 3624–3648, https://doi.org/10.1175/JCLI-D-11-00015.1.

Santer, B. D., and Coauthors, 1996: A search for human influences on the thermal structure of the atmosphere. *Nature*, **382**, 39–46, https://doi.org/10.1038/382039a0.

Scaife, A. A., and D. Smith, 2018: A signal-to-noise paradox in climate science. *npj Climate Atmos. Sci.*, **1**, 28, https://doi.org/10.1038/s41612-018-0038-4.

Screen, J. A., and I. Simmonds, 2014: Amplified mid-latitude planetary waves favour particular regional weather extremes. *Nat. Climate Change*, **4**, 704–709, https://doi.org/10.1038/nclimate2271.

Sen, P. K., 1968: Estimates of the regression coefficient based on Kendall's tau. *J. Amer. Stat. Assoc.*, **63**, 1379–1389, https://doi.org/10.1080/01621459.1968.10480934.

Serreze, M., A. Barrett, J. Stroeve, D. Kindig, and M. Holland, 2009: The emergence of surface-based Arctic amplification. *Cryosphere*, **3**, 11–19, https://doi.org/10.5194/tc-3-11-2009.

Shaw, T., and A. Voigt, 2015: Tug of war on summertime circulation between radiative forcing and sea surface warming. *Nat. Geosci.*, **8**, 560–566, https://doi.org/10.1038/ngeo2449.

Stott, P. A., S. F. B. Tett, G. S. Jones, M. R. Allen, J. F. B. Mitchell, and G. J. Jenkins, 2000: External control of 20th century temperature by natural and anthropogenic forcings. *Science*, **290**, 2133–2137, https://doi.org/10.1126/science.290.5499.2133.

——, D. A. Stone, and M. R. Allen, 2004: Human contribution to the European heatwave of 2003. *Nature*, **432**, 610–614, https://doi.org/10.1038/nature03089.

Stroeve, J. C., M. C. Serreze, M. M. Holland, J. E. Kay, J. Malanik, and A. P. Barrett, 2012: The Arctic's rapidly shrinking sea ice cover: A research synthesis. *Climatic Change*, **110**, 1005–1027, https://doi.org/10.1007/s10584-011-0101-1.

Suarez-Gutierrez, L., S. Milinski, and N. Maher, 2021: Exploiting large ensembles for a better yet simpler climate model evaluation. *Climate Dyn.*, **57**, 2557–2580, https://doi.org/10.1007/s00382-021-05821-w.

Sun, C., and Coauthors, 2019: Spring Aleutian low weakening and surface cooling trend in northwest North America during recent decades. *J. Geophys. Res. Atmos.*, **124**, 12 078–12 092, https://doi.org/10.1029/2019JD031405.

——, Y. Liu, and J. Zhang, 2020: Roles of sea surface temperature warming and loss of Arctic sea ice in the enhanced summer wetting trend over northeastern Siberia during recent decades. *J. Geophys. Res. Atmos.*, **125**, e2020JD032557, https://doi.org/10.1029/2020JD032557.

Sutton, R. T., and D. L. Hodson, 2005: Atlantic Ocean forcing of North American and European summer climate. *Science*, **309**, 115–118, https://doi.org/10.1126/science.1109496.

——, B. Dong, and J. M. Gregory, 2007: Land/sea warming ratio in response to climate change: IPCC AR4 model results and comparison with observations. *Geophys. Res. Lett.*, **34**, L02701, https://doi.org/10.1029/2006GL028164.

Teng, H., and G. Branstator, 2012: A zonal wavenumber 3 pattern of Northern Hemisphere wintertime planetary wave variability at high latitudes. *J. Climate*, **25**, 6756–6769, https://doi.org/10.1175/JCLI-D-11-00664.1.

——, ——, H. Wang, G. A. Meehl, and W. M. Washington, 2013: Probability of US heat waves affected by a subseasonal planetary wave pattern. *Nat. Geosci.*, **6**, 1056–1061, https://doi.org/10.1038/ngeo1988.

Tett, S. F., and Coauthors, 2002: Estimation of natural and anthropogenic contributions to twentieth century temperature change. *J. Geophys. Res. Atmos.*, **107**, 4306, https://doi.org/10.1029/2000JD000028.

Ting, M., 1996: Steady linear response to tropical heating in barotropic and baroclinic models. *J. Atmos. Sci.*, **53**, 1698–1709, https://doi.org/10.1175/1520-0469(1996)053<1698:SLRTTH>2.0.CO;2.

Tomczyk, A. M., M. Półrolniczak, and E. Bednorz, 2017: Circulation conditions' effect on the occurrence of heat waves in western and southwestern Europe. *Atmosphere*, **8**, 31, https://doi.org/10.3390/atmos8020031.

Wallace, J., and N.-C. Lau, 1985: On the role of barotropic energy conversions in the general circulation. *Advances in Geophysics*, Vol. 28, Elsevier, 33–74.

Wu, Q., L. Cheng, D. Chan, Y. Yao, H. Hu, and Y. Yao, 2016: Suppressed midlatitude summer atmospheric warming by

Arctic sea ice loss during 1979–2012. *Geophys. Res. Lett.*, **43**, 2792–2800, https://doi.org/10.1002/2016GL068059.

Wu, Z. W., Z. H. Jiang, J. P. Li, S. Zhong, and L. Wang, 2012a: Possible association of the western Tibetan Plateau snow cover with the decadal to interdecadal variations of northern China heatwave frequency. *Climate Dyn.*, **39**, 2393–2402, https://doi.org/10.1007/s00382-012-1439-4.

——, H. Lin, J. P. Li, Z. H. Jiang, and T. T. Ma, 2012b: Heat wave frequency variability over North America: Two distinct leading modes. *J. Geophys. Res.*, **117**, D02102, https://doi.org/10.1029/2011JD016908.

Zhang, R., and Coauthors, 2019: A review of the role of the Atlantic meridional overturning circulation in Atlantic multidecadal variability and associated climate impacts. *Rev. Geophys.*, **57**, 316–375, https://doi.org/10.1029/2019RG000644.

Zhou, L., H. Chen, and Y. Dai, 2015: Stronger warming amplification over drier ecoregions observed since 1979. *Environ. Res. Lett.*, **10**, 064012, https://doi.org/10.1088/1748-9326/10/6/064012.

——, ——, W. Hua, Y. Dai, and N. Wei, 2016: Mechanisms for stronger warming over drier ecoregions observed since 1979. *Climate Dyn.*, **47**, 2955–2974, https://doi.org/10.1007/s00382-016-3007-9.

Zhou, Y., and Z. Wu, 2016: Possible impacts of mega-El Niño/Southern Oscillation and Atlantic Multidecadal Oscillation on Eurasian heatwave frequency variability. *Quart. J. Roy. Meteor. Soc.*, **142**, 1647–1661, https://doi.org/10.1002/qj.2759.